Energy 65 (2014) 621–630

Contents lists available at ScienceDirect

Energy

journal homepage: www.elsevier.com/locate/energy

Moving beyond the limits of mass transport in liquid absorbent microfilms through the implementation of surface-induced vortices

Sajjad Bigham, Dazhi Yu, Devesh Chugh, Saeed Moghaddam*

Department of Mechanical and Aerospace Engineering, University of Florida, Gainesville, FL 32611, United States

ARTICLE INFO

Article history:
Received 13 September 2013
Received in revised form
18 November 2013
Accepted 24 November 2013
Available online 23 December 2013

Keywords:
Absorption refrigeration system
Membrane-based absorption
Absorption/desorption cycle
Thin film absorption
Lithium bromide

ABSTRACT

The slow diffusion of an absorbate molecule into an absorbent often makes the absorption process a rate-limiting step in many applications. In cases involving an absorbate with a high heat of phase change, such as water absorption into a LiBr (lithium bromide) solution, the absorption rate is further slowed due to significant heating of the absorbent. Recently, it has been demonstrated that constraining a LiBr solution film by a hydrophobic porous structure enables manipulation of the solution flow thermohydraulic characteristics. Here, it is shown that mass transport mode in a constrained laminar solution flow can be changed from diffusive to advective. This change in mode is accomplished through stretching and folding the laminar streamlines within the solution film via the implementation of micro-scale features on the flow channel surface. The process induces vortices within the solution film, which continuously bring concentrated solution from the bottom and middle of the solution channel to its interface with the vapor phase, thus leading to a significant enhancement in the absorption rate. The detailed physics of the involved transport processes is elucidated using the LBM (Lattice Boltzmann Method).

Published by Elsevier Ltd.

1. Introduction

The absorption of species into a liquid is a widely utilized process in many technologies, such as absorption heat pumps [1–9], liquid desiccant-based dehumidification [10–15], purification of the natural gas streams involving separation of CO_2 and H_2S [16,17], removal of CO_2 from flue gas [18–22], and bioreactors in which gaseous products are absorbed into a liquid phase for processing/conversion by microorganisms [23]. The absorption process in these applications is often limited by the slow rate of absorbate diffusion into the absorbent. In addition, thermal diffusion limits could further slow the absorption of an absorbate with a high heat of phase change, for example, in absorption of water vapor into a LiBr (lithium bromide) solution. If the significant amount of heat released at the vapor–liquid interface, due to phase change, is not removed (i.e. the interface is not cooled), the temperature and equilibrium water vapor pressure of the interface increase. The increase in water vapor pressure subsequently lowers the rate of water vapor absorption.

Enhancing the water vapor absorption rate into the LiBr solution has been the subject of studies [24–37] focused on advancing the falling film absorption technology. Nasr and Moghaddam [3] provide an overview of these studies and discuss the fact that, despite many efforts, tangible results have not been achieved due to the challenges of controlling thermohydraulic characteristics of a falling LiBr solution film. Recently, Yu et al. [2] numerically studied absorption characteristics of LiBr solution flows, and determined that heat and mass transfer limits in a LiBr solution flow could be enhanced if the flow channel thickness is maintained within a few hundred microns while the flow velocity is increased. Implementation of a thin solution flow reduces the heat diffusion path to the cooling surface beneath the solution film, and increasing the solution flow velocity limits the concentration boundary layer thickness. In a subsequent experimental study, Nasr and Moghaddam [3] demonstrated that a LiBr solution flow could be constrained by superhydrophobic nanofibrous membranes, and its absorption characteristics could be manipulated through independent control of the flow thickness and velocity. Through this approach, a significant increase in absorption rate versus the falling film absorption technology was achieved.

Nasr and Moghaddam [3] experimentally demonstrated the benefits of implementing a solution film at thicknesses on the order of 100 μm. To ease the manifolding burden of an absorber utilizing such a thin solution flow channel and enhance the utility of the membrane-based technology for absorbers with larger capacities, it is desirable to reduce the flow pressure drop by increasing the solution channel thickness. Note that flowing a fixed amount of mass through, for example, a 100-μm-thick channel results in approximately 125 times

* Corresponding author.
E-mail address: saeedmog@ufl.edu (S. Moghaddam).

0360-5442/$ – see front matter Published by Elsevier Ltd.
http://dx.doi.org/10.1016/j.energy.2013.11.068

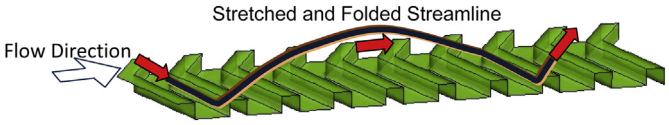

Fig. 1. A 3D schematic showing surface features and a fluid particle trajectory (i.e. a streamline) as it enters and exits the spacing between the surface features and generates a z-direction velocity component.

higher pressure drop compared to a 500-μm-thick channel, since the laminar flow pressure drop is proportional to V/D_h^2. However, increasing the solution channel thickness also reduces the absorption rate, since transport within the solution flow is governed by the laminar flow theory, and molecular diffusion is the sole mechanism for the absorbed molecule to be transported into the bulk absorbent. Thus, the solution flow should be mixed in order to achieve high absorption rates.

The microfluidic literature provides a rich body of research on ways to mix laminar flow in microchannels. The methodologies demonstrated in various approaches involve either active or passive components. Active mixers such as piezoelectric [38] and magneto/electro-hydrodynamic [39] actuation and pressure perturbations [40] put extra burden on the system hardware. In addition, the utility, robustness, and reliability of such approaches for this application could be questioned. From among different mixing techniques, we consider a passive approach utilized by Stroock et al. [41] quite suitable for this application. The method involves generating chaotic advection [42] within the flow through stretching and folding the laminar streamlines (cf. Fig. 1).

This study explores the utility of this approach to membrane-based absorption technology [3–5]. A set of numerical simulations is conducted to evaluate the performance of a membrane-based absorber, utilizing LiBr solution and water as the absorbent and absorbate, respectively. First, we discuss the heat and mass transport and absorption characteristics of a 0.5 mm thick LiBr solution film constrained by a membrane, as a base case. Then, we implement microscale features on the bottom of the solution channel to induce vortices and investigate their effects on transport within the absorbent layer. Finally, we analyze the effect on the absorption rate of placing thermally conducting walls at the side boundaries of the flow (implemented for better cooling of the solution flow).

2. Experiment

An experimental study is conducted to verify the numerical method. This section provides a brief overview of the experimental setup and measurement procedure and uncertainties. Further details on the experimental setup, test procedure, and uncertainty analysis are provided in Refs. [3–5].

2.1. Experimental setup

Fig. 2 depicts a photograph of the experimental setup. The experimental loop consists of a LiBr solution line and a refrigerant (water) line. The solution line consists of an absorber, desorber, pump, filter, solution reservoir, Coriolis mass flow meter, and two solution heat exchangers. A photograph of the absorber heat exchanger with a PTFE (polytetrafluoroethlyene) membrane bonded over its surface is shown in Fig. 3. The water line consists of an evaporator, condenser, Coriolis mass flow meter, and a water reservoir. In the solution line, a micro gear pump (HNP Mikrosysteme, Germany) drives the weak LiBr solution to a Coriolis mass flow meter (Bronkhorst, USA) and then through a solution heat exchanger where the solution is preheated to a desired temperature before entering the desorber. In the desorber, the weak LiBr solution is heated by a thin film heater (Omega Engineering, CT) to desorb water. The desorbed water vapor flows to a condenser and the strong LiBr solution leaves the desorber and flows through a heat exchanger, where it is cooled to a preset temperature before it enters the absorber. The condensed water leaves the condenser and flows through a Coriolis mass flow meter (Micro Motion, CO) to the evaporator, where it is vaporized and supplied back to the absorber. The strong solution flows through the absorber and absorbs the water vapor generated in the evaporator. The weak solution leaving the absorber flows through a filter and is pumped back to the solution pre-heater and then to the desorber to complete the cycle. The desorber and evaporator heat exchangers are heated by flexible heaters. The experimental loop is also equipped with two small reservoirs with sight glass to monitor the liquid in the solution and in the water lines. These reservoirs also serve as compensation chambers and assist in proper charging of the loop. The data are measured by pressure transducers, thermocouples, and mass flow meters and are recorded by a data acquisition system.

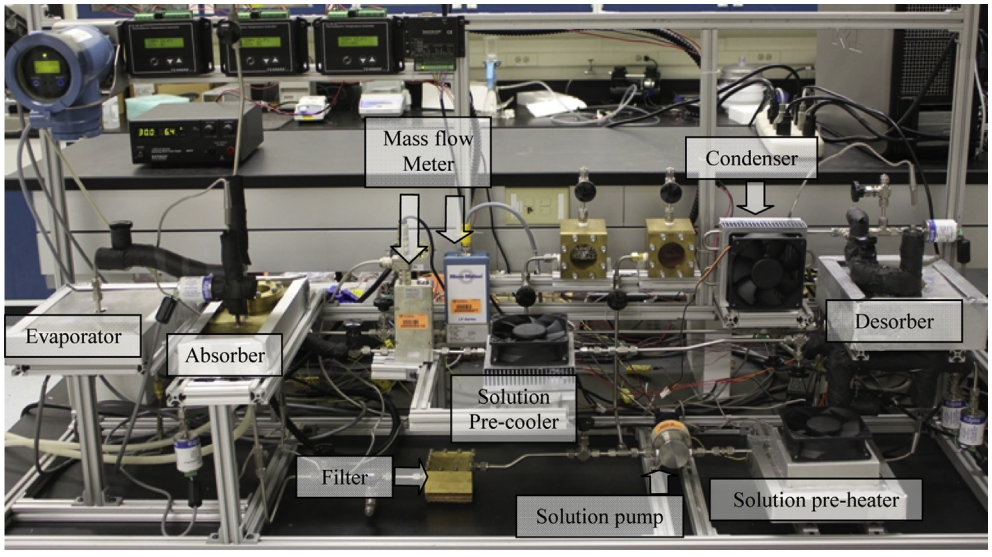

Fig. 2. A photograph of the assembled experimental setup.

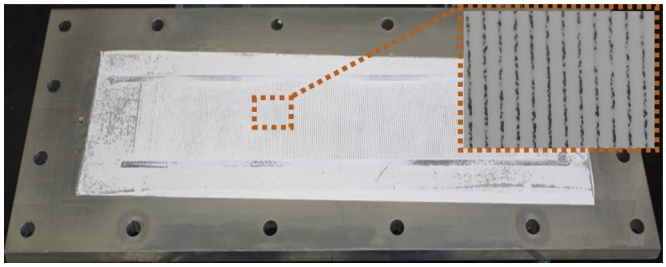

Fig. 3. A photograph of the absorber heat exchanger with a PTFE membrane bonded over its surface (Bonding method is described in Mortazavi and Moghaddam [43]).

2.2. Experimental procedure and uncertainty

The system solution loop was charged with a 55% LiBr solution inhibited by Lithium Molybdate (Leverton-Clarke Ltd., UK). The water line was charged with degassed and deionized water. Each experimental run began by operating the solution pump and setting the flow rate to a desired value. The water chiller was then turned on and the temperature of the absorber cooling water was set. A valve between the evaporator and absorber was then opened to begin the absorption process. Next, the TEC (Thermo Electric Cooler) modules were turned on and the inlet temperatures to the absorber and desorber heat exchanges were set. Once the desired temperatures were reached, the desorber and evaporator heaters were powered on. Changes in temperatures, pressures, and mass flow rates were monitored continuously. The system was assumed to have reached steady-state when variations in the absorber pressure and the solution density were within 10 Pa and 5 kg/m^3, respectively, for at least 30 min. The absorption rate was then directly measured by the water line mass flow meter.

The accuracy of the water mass flow meter that directly measures the water absorption rate is ±1%. However, due to the unsteady nature of the condensate flow, a fluctuation of up to ±5% was recorded during the experiment. The reported absorption rates are the average of the measured values over a period of time, after the system reached a steady state. The concentration uncertainty is calculated using the following equation:

$$\Delta X = \sqrt{\left(\frac{\partial X}{\partial \rho}\Delta\rho\right)^2 + \left(\frac{\partial X}{\partial T}\Delta T\right)^2}$$

where X and T are the solution concentration and temperature, respectively, and ρ is the solution density. Table 1 lists uncertainty in all measurements.

Table 1
Variable uncertainties.

Variable	Uncertainty
Pressure	0.5%
Density (kg/m^3)	5 kg/m^3
Absorption rate	5%
Solution flow rate	0.2%
Temperature (°C)	0.3 °C

3. Numerical simluation

3.1. Governing equations

To formulate the problem, a continuum-based approach is used. Fluid flow is considered to be steady, laminar, and incompressible. The governing equations can be written as:

$$u_j\frac{\partial u_i}{\partial x_j} = -\frac{1}{\rho}\frac{\partial p}{\partial x_i} + \nu\frac{\partial u_i}{\partial x_j \partial x_j} \quad (1)$$

$$u_j\frac{\partial T_i}{\partial x_j} = -\alpha\frac{\partial T}{\partial x_j \partial x_j} \quad (2)$$

$$u_j\frac{\partial X}{\partial x_j} = -D\frac{\partial X}{\partial x_j \partial x_j} \quad (3)$$

where u is the velocity, ρ is the solution density, ν is the kinematic viscosity, p is the fluid pressure, T is the solution temperature, α is the thermal diffusivity, X is the solution concentration and D is the mass diffusivity.

In a membrane-based absorber, the vapor has to pass through the membrane pores before interacting with the LiBr solution. Flow through a porous membrane can be classified as viscous, transitional, or free molecular flow regimes depending on the magnitude of the Knudsen (Kn) number. Kn number is defined as the ratio of the mean free path (λ) to the pore diameter (d_p):

$$Kn = \frac{\lambda}{d_p} \quad (4)$$

The mean free path is given by Ref. [44]:

$$\lambda = \frac{k_b T}{\sqrt{2}\pi d^2 p} \quad (5)$$

where k_b is the Boltzmann constant, T is the absolute temperature, d is the molecular diameter, and p is the vapor pressure. To calculate the mass flux through the membrane, the flow regime must be first determined. Beskok and Karniadakis [45] classified the flow regime as free molecular regime for $Kn > 10$ and as transitional flow regime for $0.1 < Kn < 10$. The vapor pressure at 5 °C (the operating temperature of a typical evaporator) is 873 Pa. The diameter of the water molecule is 2.7×10^{-10} m. Using these values, we calculate a water molecule mean free path of 13 μm. Since the optimal membrane pore size for this application is expected to be less than 1 μm (membranes with this pore size range have a reasonable liquid breakthrough pressure for this application [3]), the vapor flow through the membrane pores falls in the transitional or free molecular flow regime. According to the Dusty-Gas model [46], the mass transfer through a membrane consists of diffusion and viscous fluxes. The molar diffusion flux is given by:

$$N^D = D_e^k\frac{-1}{RT}\Delta p \quad (6)$$

$$D_e^k = \frac{2\varepsilon r}{3\tau}\sqrt{\frac{8RT}{\pi M}} \quad (7)$$

where R is the gas constant, M is the molecular weight, r is the pore radius, ε is the membrane porosity, and τ is the membrane tortuosity. The molar viscous flux is given by:

$$N^V = \frac{-p}{RT\mu}\frac{\varepsilon r^2}{8\tau}\Delta p \quad (8)$$

where μ is the viscosity and p is the pressure. The total mass flux through the membrane pores can be written as the sum of the diffusion and viscous fluxes:

$$N = N^D + N^V \quad (9)$$

The vapor mass flux through the membrane can be then computed from Ref. [2]:

$$J = k_m(p_v - p_i),\ k_m = -\frac{M}{\delta_m}\left(\frac{D_e^k}{RT} + \frac{pB_0}{RT\mu}\right) \quad (10)$$

where k_m is the membrane mass transfer coefficient or permeability, p_v is the water vapor pressure, p_i is the water vapor pressure of the solution at the interface and δ_m is the membrane thickness.

To evaluate the accuracy of Eq. (10), permeability of nanofibrous membranes with different pore sizes were experimentally measured. Tests were performed at a flow rate of up to 0.01 kg m^{-2} s^{-1} and an absolute pressure of 0.85 kPa. The results, provided in Ref. [5], are within 5% of Eq. (10) predictions. Also, experimental studies on a membrane-based absorber by Isfahani and Moghaddam [3] suggested that a nanofibrous membrane with a pore size of 1 μm has a relatively low pressure drop compare to the overall pressure potential that drives the absorption process. Measurements on a 160-μm-thick solution film over an absorption rate of 0.002–0.006 kg m^{-2} s^{-1} suggested that the dominant resistance is mass transfer through the solution ($P_i - P_s$) and membranes contributes approximately 20% to the overall resistance.

At the membrane surface, it is supposed that the LiBr solution and the vapor are at an equilibrium state. Mass flux across the membrane compared to mass flux along the channel as well as heat transferring to the vapor phase through the membrane are all assumed to be negligible. Therefore, at the membrane surface, the following heat and mass boundary conditions are used [2,29,47–49]:

$$k(T, X)\frac{\partial T}{\partial n} = h(T, X).k_m(p_v - p_i(T, X)) \quad (11)$$

$$D(T, X).\ \rho(T, X)\frac{\partial X}{\partial n} = k_m(p_v - p_i(T, X)) \quad (12)$$

where h is the latent heat of evaporation, ρ is the solution density, and n is the interface normal direction. The LiBr properties are provided by McNeely [50].

No-slip and no-flux boundary conditions are used for momentum and the concentration equations respectively at the cooling surface. A linear temperature distribution is used at the cooling surface. The temperature and concentration are specified at the inlet, while a zero gradient boundary condition was used for both the temperature and concentration at the outlet. Also, symmetric conditions are applied on the sides of the flow domain.

3.2. Numerical solution

To solve the governing equations with the mentioned boundary conditions, an in-house computational fluid dynamics solver based on the LBM (Lattice Boltzmann Method) and a finite difference method for the concentration and temperature fields are used. A detailed description of the code is provided in Yu and Ladd [51].

In the LBM, the fluid is simulated by fictive particles with a mass distribution function of $f(\vec{x}, \vec{e}, t)$. To predict the motion of these particles, the Boltzmann equation is solved over a discrete lattice mesh. The popular SRT (single relaxation time) model, with the time step δt and space step $e_\alpha \delta t$, is:

$$f_\alpha(X_i + e_\alpha\delta t, t + \delta t) - f_\alpha(X_i, t) = -\frac{1}{\lambda}\left[f_\alpha(X_i, t) - f_\alpha^{(eq)}(X_i, t)\right] \quad (13)$$

where e_α is the discrete particle velocity set, λ the normalized relaxation time, and X_i a point in the discretized physical space. Eq. (13) is in fact the discrete lattice Boltzmann equation [52] with BGK approximation [45]. The viscosity in the N–S equation derived from Eq. (13) is:

$$\nu = \left(\lambda - \frac{1}{2}\right)c_s^2\delta t \quad (14)$$

where C_s is the speed of sound. This choice of the viscosity makes formally the LBGK scheme a second order method for solving incompressible flows [53]. The positivity of the viscosity requires that $\lambda > 0.5$. In Eq. (13), $f_\alpha(X_i, t)$ is the discretized distribution function associated with the α-th discrete velocity e_α and $f_\alpha^{(eq)}$ is the corresponding equilibrium distribution function.

The macroscopic quantities (such as mass density ρ and momentum density $\rho\vec{u}$) can be obtained by evaluating the hydrodynamic moments of the distribution function f as follows:

$$\rho = \sum_\alpha f_\alpha^{eq} \quad (15)$$

$$\rho\vec{u} = \sum_\alpha f_\alpha^{eq}\vec{e}_\alpha \quad (16)$$

For a more detailed discussion about LBM, the readers are referred to a prior publication [53].

The grid dimensions of the computational domain were 5 μm in all three directions. A grid independence study was performed to ensure that the computational results are independent of the grid size. The maximum error in the absorption rate was found to be less than 2% when the grid size was reduced by a factor of 2.

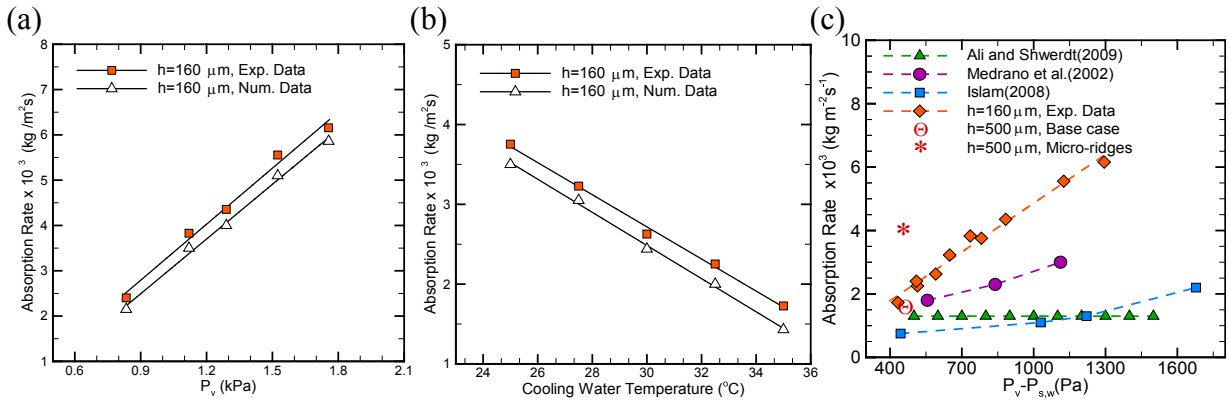

Fig. 4. Absorption rate as a function of vapor pressure (a) and cooling water temperature (b); comparison of absorption rate, as a function pressure potential, with those of other studies (c).

Table 2
Input parameters of the numerical model.

Parameter	Value
Vapor saturation temperature, T_v	5 °C
Inlet solution temperature, T_i	32.5 °C
Inlet solution concentration, C_i	60%
Solution mean velocity, $\overline{u}$	0.05 m/s
Membrane porosity, ε	60%
Membrane pore diameter, d_m	1 μm
Tortuosity, τ	1.0
Membrane thickness, δ_m	20 μm
Absorbent channel height, CH	500 μm
Channel length, L	600 mm

4. Experimental results and verification of numerical model

First, the water vapor pressure was increased while the other test parameters were kept constant (at a nominal set of values [3]). Fig. 4a shows the effect of water vapor pressure on the absorption rate. The results clearly show that increasing the water vapor pressure (P_v) linearly increases the absorption rate. In a second test, the solution water vapor pressure ($P_{s,w}$) was changed while the vapor pressure was kept constant. The solution water pressure varies with the solution temperature and concentration. In this test, the change in the solution water pressure was achieved by varying the solution channel wall temperature from 25 to 35 °C in 2.5 °C increments. All other test conditions were kept constant at a nominal set of values [3]. The results (cf. Fig. 4b) showed a linear decrease in absorption rate with an increase in solution temperature (i.e. increase in the solution water vapor pressure). All absorption rates reported in Fig. 4a and b are normalized with respect to the pressure potential ($P_v - P_s$) and plotted in Fig. 4c. The solution water pressure used in the calculation is the average of the absorber inlet and exit. The results suggest that the absorption rate linearly increased with the pressure potential regardless of the source of change in pressure.

Fig. 4a and b also compare the numerical results with the experimental data showing an overall agreement within 15%. This difference between the numerical and experimental results could be mainly due to uncertainty in the film thickness, potential inaccuracy in the solution water vapor pressure correlations used in numerical simulations and non-uniform wall temperature in the experiment.

5. Results and discussion

The validated numerical model is then used to analyze the impact of chaotic advection on absorption characteristics of a thick absorbent flow constrained by a membrane. Table 2 lists the input parameters to the model. The temperature of the channel bottom wall was set to vary linearly from 27.5 °C at the solution outlet to 32.5 °C at the solution inlet, in order to resemble a counter flow heat exchanger configuration.

5.1. Base case

Fig. 5a provides the concentration contours within the flow channel. A scale factor of 0.005 is used in the x direction to show the entire flow domain. The absorbate (water vapor) is absorbed into the absorbent (LiBr solution) at the membrane–absorbent interface (i.e. the top surface of the model). As the solution flows through the channel, the thickness of the concentration boundary layer formed at the interface increases. The boundary layer acts as a resistance to mass transfer between the interface and the bulk of the solution. The results clearly suggest that most of the solution is not involved in the absorption process and leaves the channel at a high concentration.

To further explain the results, variations of the bulk and interface concentrations along the channel are plotted in Fig. 6. At the channel inlet, a high solution concentration (and therefore a low water vapor pressure in the solution phase) results in rapid absorption of the water vapor into the solution. This high absorption rate results in a sharp decline in the solution concentration at the interface. However, due to the low diffusion rate of the water molecules through the solution, this change is not reflected within the bulk flow. While the interface concentration decreases by 6.2% (from 60% to 53.8%) over the 600 mm length of the channel, the bulk concentration decreases by only 1.2% (from 60% to 58.8%) over the same length.

Fig. 5b depicts temperature distribution within the flow. The results show a sudden increase in temperature of the interface ($T_{interface}$) at the channel inlet. This increase in temperature is due to the release of a significant amount of heat as a result of a high absorption rate. As mentioned earlier, a high solution concentration at the inlet is responsible for the high rate of absorption. This high absorption rate also results in a sizeable increase in the bulk

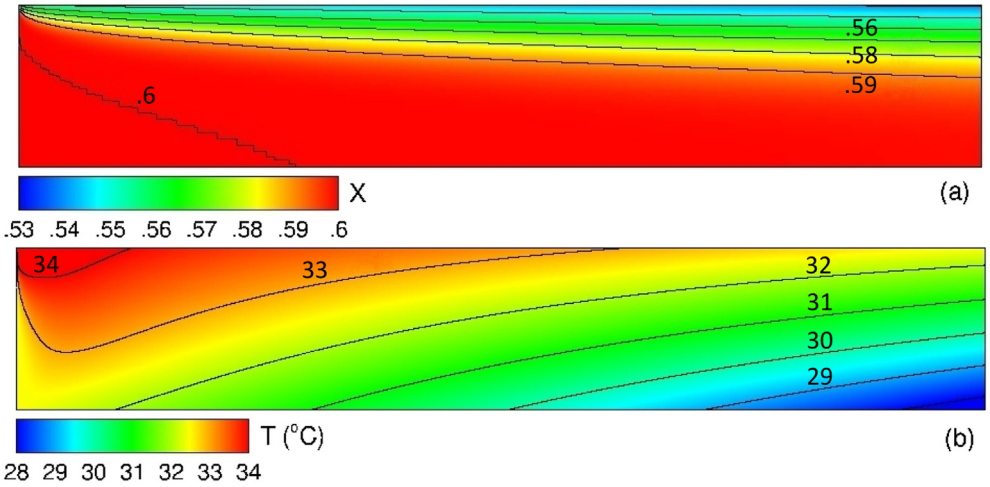

Fig. 5. LiBr solution concentration (a) and temperature (b) contours within a 500-micron-thick and 600-mm-long flow channel. Table 2 provides parameters used as input to the simulation.

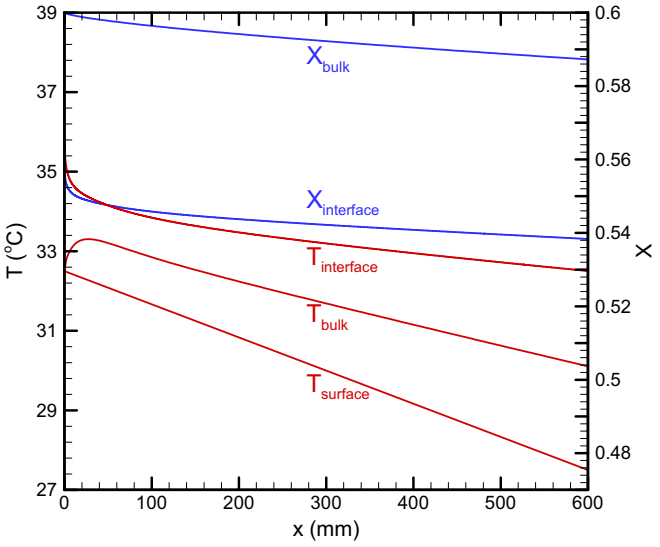

Fig. 6. Variations of temperature and concentration at the interface and within the bulk along the flow channel.

temperature (T_{bulk}) at the channel inlet. However, the relatively high heat diffusion rate in the LiBr solution results in rapid cooling of the interface. Thereafter, both the interface and the bulk temperatures closely follow the cooling surface temperature. Comparisons between the interface and bulk values of the temperature and concentration profiles clearly indicate that the absorption process in this solution is mass-transfer limited.

Fig. 7 depicts the water vapor absorption rate into the solution film. The highest absorption rate is achieved at the channel inlet. This is due to the high concentration of the solution at the inlet. The absorption rate thereafter declines as the concentration boundary layer near the vapor–solution interface grows. The average absorption rate over the entire channel length is 0.0016 kg/m^{2}s (cf. Fig. 4c).

5.2. Implementation of surface-induced vortices

The heat and mass transfer process discussed in the previous section (i.e. the base case) is diffusion dominated, since the flow is laminar ($Re = 7$). As mentioned in the introduction section, the approach utilized here to overcome diffusion limitations involves incorporation of staggered herringbone structures (hereafter called "ridges") on the flow channel bottom wall. The ridges generate anisotropic resistance to the absorbent flow, which stretches and twists a portion of the absorbent flow volume. A parametric study is conducted to determine the optimal ridge geometry for a membrane-based absorber. Table 3 provides the list of variables and their range used in the numerical simulations. The variables RH, CH, S, α, P and J listed in the table are the ridge height, channel height, distance between the ridges in the x-direction, ridge angle with respect to the x-axis, ridge length in the y-direction, and the absorption rate, respectively. The simulation results clearly suggested that relatively shallow ridges (e.g. 100-μm-deep, RH/CH = 0.2) have little impact on the absorption rate. The results indicate that the ridges height should be more than 0.5 times the main channel height (i.e. aspect ratio of RH/CH > 0.5) so that the induced surface vortices can produce sufficient momentum to impact the main flow and continuously replenish the interface with a concentrated solution. Comparison of the absorption rate between cases with a RH of 100, 300, and 500 μm shows that increasing the ridges depth directly enhances the absorption rate. However, the current scalable and economical micro-manufacturing technologies have limitations in producing deep ridges. In the wet etching process utilized here a depth to width ratio of more than one cannot be achieved. For this reason, a ridge height of 300 μm is selected. Comparison of other simulated geometries shows that the maximum performance is achieved at $\alpha = 30°$, $S = 600$ μm, and $P = 660$ μm. It is also determined that ridges with long and short arms alternated after approximately 40 ridges (cf. Fig. 8) produce a higher absorption rate. This will become evident when the physics of the mixing process is discussed in the following sections.

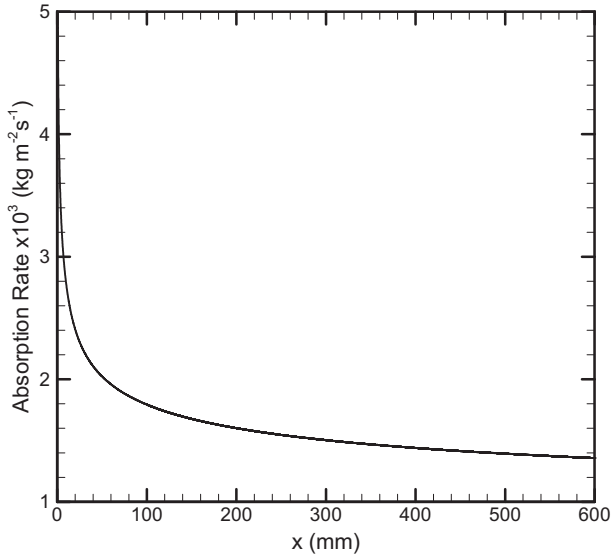

Fig. 7. Variations of absorption rate along the solution channel.

Fig. 9 illustrates how the surface induced vortices control the concentration distribution within the flow. At any given cross-section two vortices are formed, one on each arm of the ridge. The concentration contours indicate that the low concentration solution at the vapor–liquid interface is advected down towards the bottom of the channel by the transverse velocity generated by the vortices. Switching between the ridges (cf. Fig. 8) reorganizes the vortices across the cross-section and mixes the low concentration solution with a higher concentration solution formed at the center of the larger vortex. The concentration contours shown at different cross-sections of the flow channel (cf. Fig. 9) illustrate this process.

Fig. 10 shows the y and z components of the velocity vector along the microchannel at $y = 180$ μm and $z = 750$ μm (i.e. 50 μm below the vapor–liquid interface). The results clearly show a major difference (approximately 4–5 times) between the y component of the velocity on the long and short ridges. The maximum transverse velocity in y direction occurs on the long arm of the ridges and the average value of y-velocity is 1.4 mm/s, which is 12% of the x component of the velocity.

Table 3
Effect of the ridge geometry on the absorption rate.

RH (μm)	RH/ChH	S (μm)	α (°)	P (μm)	$J \times 10^3$ (kg m^{-2} s^{-1})
100	0.2	500	45	500	2
300	0.6	500	45	500	3.4
500	1	500	45	500	3.7
300	0.6	600	45	500	3.5
300	0.6	800	45	500	3.4
300	0.6	600	30	500	3.7
300	0.6	600	15	500	3.1
300	0.6	600	30	660	4
300	0.6	600	30	1320	3

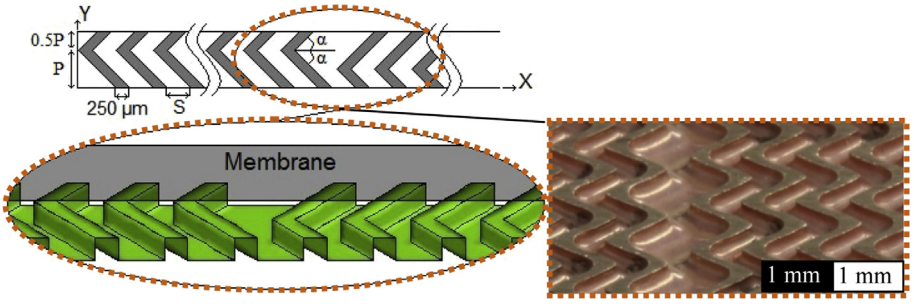

Fig. 8. A top view and 3D schematics of a flow channel showing the ridges on the channel bottom wall along with herringbone structures made of cupper through wet etching process.

Fig. 11a depicts the concentration contours at $Y = 180$ μm cross section. The results clearly illustrate how the implementation of the ridges substantially changes the concentration distribution in the absorbent film. The solution is well mixed, and mass transfer inside the flow channel is no longer dominated by molecular diffusion. The surface induced vortices take the absorbent from the bulk flow to the vapor–liquid interface and continuously interrupt the concentration boundary layer growth. In other words, the absorbed water molecules are advected away from the interface and a high solution concentration is always maintained at the vapor–liquid interface.

The temperature contours, provided in Fig. 11b, show that the advection process also significantly impacts the temperature field. The mixing of the warmer solution from the vapor–liquid interface with the relatively cooler bulk solution distributes the interface heat throughout the bulk. However, because the diffusive heat transport mechanism is still significant, compared to the advective heat transport mechanism, a thermal gradient in the z-direction is established.

To better illustrate the role of mixing in the absorption process, variations of the interface and bulk values of the concentration and temperature are plotted in Fig. 12. The results show that, as compared to the base case (cf. Fig. 5), the bulk concentration (X_{bulk}) more closely follows the interface concentration ($X_{interface}$), with about a 2% difference through the entire channel length. The results also show a significant fluctuation (close to 0.5%) in the interface concentration. The physics of the mixing process involving the two vortices formed over the long and short arms of the ridges is responsible for this phenomenon. As mentioned earlier, the strength of the large and small vortices is significantly different. This difference in the strength of the vortices is highlighted in Fig. 10, where the y component of velocity on the long arm of the ridge is seen to be 4–5 times larger than y component of velocity over the short arm of the ridges. Reduction in the y component of the velocity (e.g. at $x = 30$ mm) slows the interface replenishment process, resulting in a decrease in the interface concentration. The interface concentration increases again when the solution flows on the long arm of the ridges (e.g. at $x = 60$ mm). This phenomenon is also responsible for fluctuations of the interface temperature.

Fig. 13 provides the results on absorption rate along the channel length. As in the base case (cf. Fig. 7), the high inlet absorption rate quickly declines within a short distance from the inlet. However, the rate of this decline is significantly slower than that of the base case. After this rapid decrease in the absorption rate, the absorption rate stabilizes at a much higher rate than that of the base case due to the fact that the modified fluid flow replenishes the vapor–liquid interface with a concentrated solution. The absorption rate also fluctuates. The increasing trend at each fluctuation reaches a maximum within a short distance, after which the absorption rate starts to decline. However, switching between the position of the short and long arms of the ridge (cf. Fig. 8) reverses the trend and the absorption rate increases again. Alternating between the two surface patterns continuously brings the concentrated solution from the middle of the vortices to the vapor–liquid interface (cf. Fig. 9). This is essential to maintaining a high absorption rate. If this alternation does not take place, the absorption rate continuously declines. Overall, the process results in an average absorption rate of 0.004 kg/m^{2}s, which is approximately 2.5 times higher than the absorption rate achieved in the base case (cf. Fig. 4c).

The enhancement in the absorption rate proportionally increases the heat release at the vapor–liquid interface. The results also show a significant fluctuation in the interface temperature. The

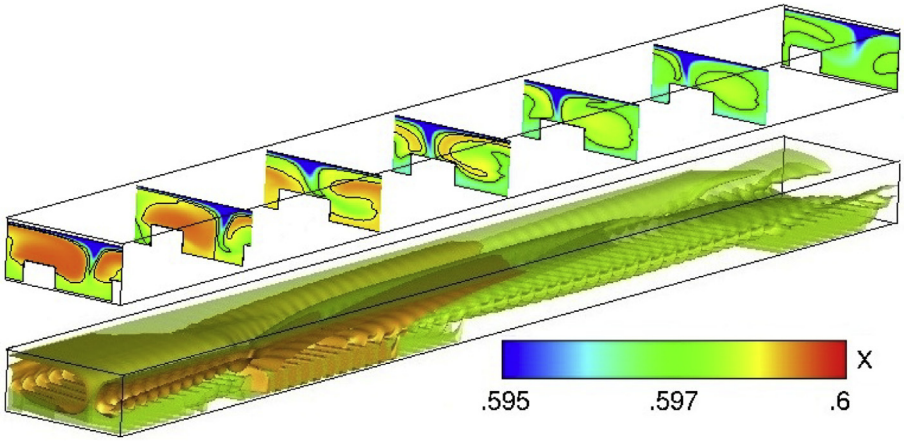

Fig. 9. A 3D view of concentration contours showing two vortices formed on the short and long arms of the micro-ridge structure.

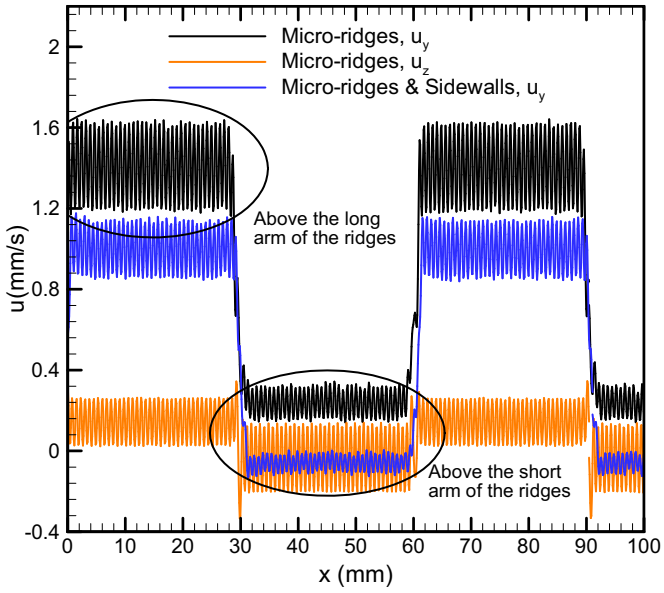

Fig. 10. Variations of the y and z components of the velocity vector along the micro-channel at $y = 180$ μm and $z = 750$ μm for channels with and without sidewalls.

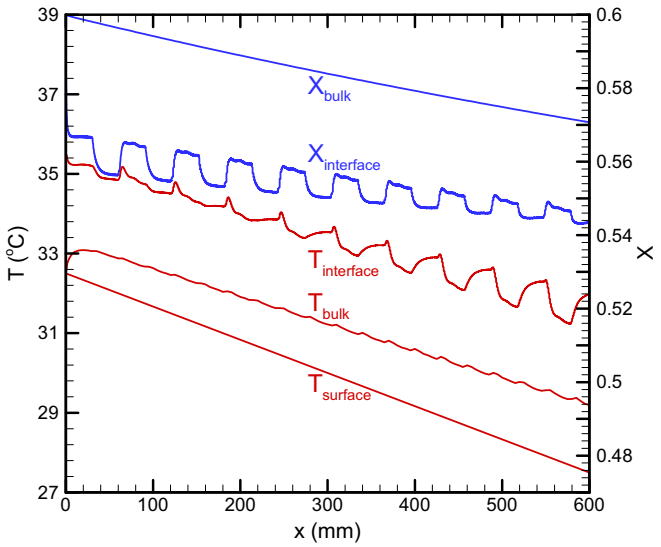

Fig. 12. Variations of temperature and concentration at the interface and within the bulk along the flow channel incorporating micro-ridges on the channel bottom wall.

amplitude of these fluctuations increases as the difference between the solution temperature at the interface and at the cooling surface increases along the channel.

5.3. Implementation of conducting sidewalls

As discussed in the previous section, implementation of the surface vortices enhanced the absorption rate. This increase in the absorption rate resulted in significant heating of the solution and increased the interface and wall temperature difference. To better cool the solution, we implement thermally conducting walls at the sides of the flow stream. Besides, the top surface of the sidewalls provides a sufficient space to bond directly the membrane on the channels (cf. Fig. 3). Fig. 14 provides the temperature and concentration profiles for this case. The results indicate that adding the sidewalls reduces the average temperature difference between the interface and cooling wall to 1.27 °C, from 3.45 °C in the case of no sidewalls. However, adding the sidewalls weakens the strength of the vortices, as evidenced by the decrease in the y component of the velocity (cf. Fig. 10). A comparison of the difference between the concentrations at the interface and bulk (cf. Fig. 14) with that presented in Fig. 12 (when no sidewall is present) suggests that adding the sidewalls increased the difference from 3.25% to 4.3%. In other words, although adding the sidewalls reduced the heat transfer resistance, it slightly increased the mass transfer resistance.

To evaluate the overall impact of adding the sidewalls, the absorption rate for this case is added in Fig. 13. A comparison of the absorption rate obtained in this case with that of the case without the sidewalls shows a decline in the absorption rate at the beginning of the channel. This decrease in absorption rate is due to a reduction in the transverse velocity. However, due to significant improvement is the solution cooling process, a better absorption rate is achieved over the second half of the channel length. Overall, adding the sidewalls results in a marginal improvement of the absorption rate to 0.0042 kg/m^{2}s.

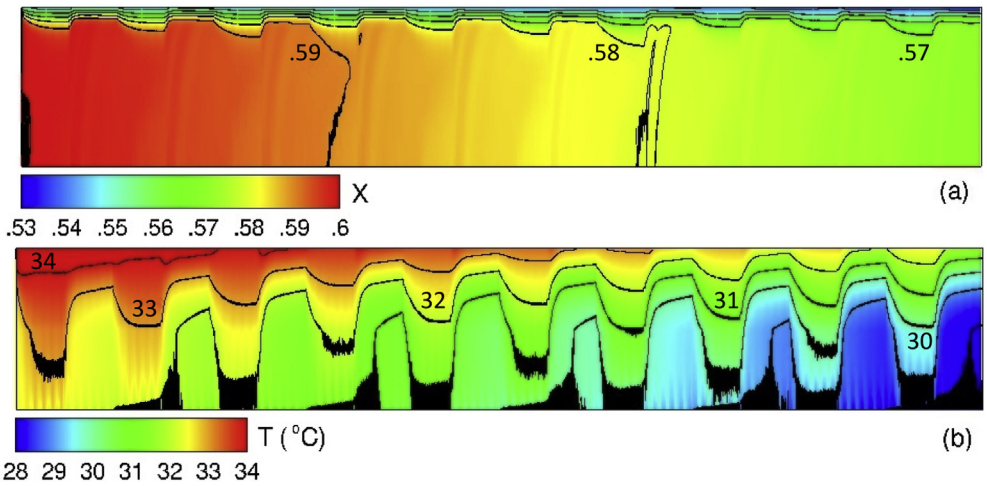

Fig. 11. LiBr solution concentration (a) and temperature (b) contours within a 500-micron-thick and 600-mm-long flow channel incorporating micro-ridges on the channel bottom wall. Table 2 provides parameters used as input to the simulation.

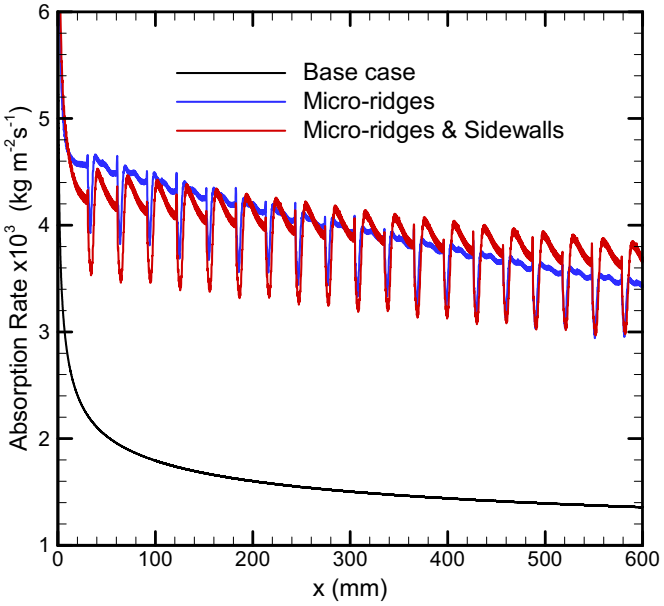

Fig. 13. Variations of the absorption rate for three cases.

6. Conclusion

The study enhanced our understanding of opportunities for improving the absorption rate in a constrained absorbent solution film. The results showed that in the case of a 500-μm-thick solution channel mass transfer rate is limited due to the formation of a thick concentration boundary layer at the vapor–liquid interface. The formation of the concentration boundary layer significantly limits the absorption rate to an average value of about 0.0016 kg/m^{2}s. Implementation of surface microstructures induces vortices within the solution flow, which changes the mass transfer regime from diffusive to advective. The vortices continuously bring concentrated solution from the bottom and middle of the solution channel to the vapor–liquid interface. As a result, the absorption rate increases by a factor of 2.5 to 0.004 kg/m^{2}s.

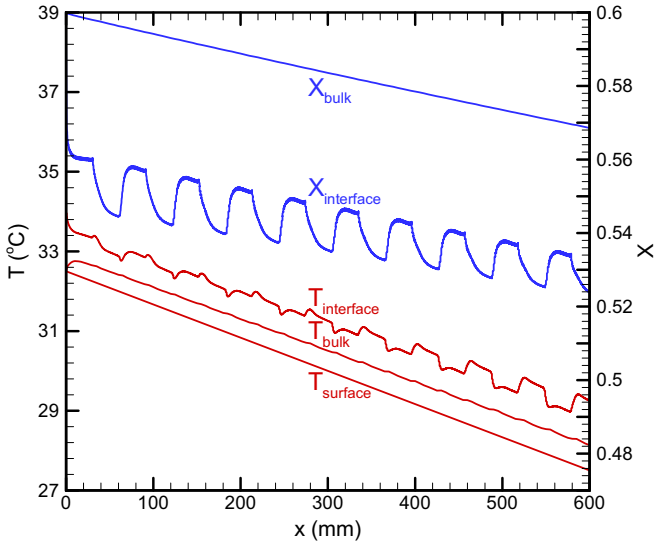

Fig. 14. Variations of temperature and concentration at the interface and in the bulk along the flow channel incorporating micro-ridges and heat conducting sidewalls.

To improve cooling of the solution flow, addition of thermally conducting sidewalls was examined. Adding the sidewalls improved the heat transfer field but hindered the surface induced vortices and increased the mass diffusion resistance. Overall, addition of the sidewalls further improved the absorption rate to 0.0042 kg/m^{2}s.

The surface-induced vortices helped to move beyond the mass diffusion limitation paradigm in absorbent films. The implemented geometry was only an example, and further enhancement of the absorption rate could be achieved through tailoring of the microstructures design. Similarly, alternative configurations could be utilized to better remove heat from the solution, particularly from the vapor–liquid interface.

Acknowledgments

The presented study was supported by a Grant from the Advanced Research Projects Agency-Energy (ARPA-E) under contract DE-AR0000133.

References

[1] Srikhirin P, Aphornratana S, Chungpaibulpatana S. A review of absorption refrigeration technologies. Renew Sustain Energy Rev 2001;5:343–72.
[2] Yu D, Chung J, Moghaddam S. Parametric study of water vapor absorption into a constrained thin film of lithium bromide solution. Int J Heat Mass Transf 2012;55:5687–95.
[3] Isfahani RN, Moghaddam S. Absorption characteristics of lithium bromide (LiBr) solution constrained by superhydrophobic nanofibrous structures. Int J Heat Mass Transf 2013;63:82–90.
[4] Isfahani RN, Fazeli A, Bigham S, Moghaddam S. Physics of lithium bromide (LiBr) solution dewatering through vapor venting membranes. Int J Multiph Flow 2014;58:27–38.
[5] Nasr Isfahani R, Sampath K, Moghaddam S. Nanofibrous membrane-based absorption refrigeration system. Int J Refrig 2013;36:2297–307.
[6] Li Y, Fu L, Zhang S, Zhao X. A new type of district heating system based on distributed absorption heat pumps. Energy 2011;36:4570–6.
[7] Izquierdo M, Marcos JD, Palacios ME, González-Gil A. Experimental evaluation of a low-power direct air-cooled double-effect LiBr–H_2O absorption prototype. Energy 2012;37:737–48.
[8] Kim YJ, Kim S, Joshi YK, Fedorov AG, Kohl PA. Thermodynamic analysis of an absorption refrigeration system with ionic-liquid/refrigerant mixture as a working fluid. Energy 2012;44:1005–16.
[9] Du S, Wang RZ, Lin P, Xu ZZ, Pan QW, Xu SC. Experimental studies on an air-cooled two-stage NH_3-H_2O solar absorption air-conditioning prototype. Energy 2012;45:581–7.
[10] Zhang L-Z, Zhang N. A heat pump driven and hollow fiber membrane-based liquid desiccant air dehumidification system: modeling and experimental validation. Energy 2013.
[11] Das RS, Jain S. Experimental performance of indirect air–liquid membrane contactors for liquid desiccant cooling systems. Energy 2013;57:319–25.
[12] Gommed K, Grossman G. Experimental investigation of a liquid desiccant system for solar cooling and dehumidification. Sol Energy 2007;81:131–8.
[13] Yin Y, Zhang X, Chen Z. Experimental study on dehumidifier and regenerator of liquid desiccant cooling air conditioning system. Build Environ 2007;42:2505–11.
[14] Abdul-Wahab SA, Zurigat YH, Abu-Arabi MK. Predictions of moisture removal rate and dehumidification effectiveness for structured liquid desiccant air dehumidifier. Energy 2004;29:19–34.
[15] Bergero S, Chiari A. On the performances of a hybrid air-conditioning system in different climatic conditions. Energy 2011;36:5261–73.
[16] Su H, Wang S, Niu H, Pan L, Wang A, Hu Y. Mass transfer characteristics of H_2S absorption from gaseous mixture into methyldiethanolamine solution in a T-junction microchannel. Sep Purif Technol 2010;72:326–34.
[17] Chmielniak T, Lepszy S, Wójcik K. Analysis of gas turbine combined heat and power system for carbon capture installation of coal-fired power plant. Energy 2012;45:125–33.
[18] Mondal MK, Balsora HK, Varshney P. Progress and trends in CO_2 capture/separation technologies: a review. Energy 2012;46:431–41.
[19] Olajire AA. CO_2 capture and separation technologies for end-of-pipe applications – a review. Energy 2010;35:2610–28.
[20] Feron PHM, Jansen AE. CO_2 separation with polyolefin membrane contactors and dedicated absorption liquids: performances and prospects. Sep Purif Technol 2002;27:231–42.
[21] Aaron D, Tsouris C. Separation of CO_2 from flue gas: a review. Sep Sci Technol 2005;40:321–48.
[22] Moller B, Genrup M, Assadi M. On the off-design of a natural gas-fired combined cycle with CO_2 capture. Energy 2007;32:353–9.

[23] Kraakman NJR, Rocha-Rios J, van Loosdrecht MCM. Review of mass transfer aspects for biological gas treatment. Appl Microbiol Biotechnol 2011;91:873–86.
[24] Islam R, Wijeysundera NE, Ho JC. Evaluation of heat and mass transfer coefficients for falling-films on tubular absorbers. Int J Refrig 2003;26:197–204.
[25] Yoon JI, Kwon OK, Moon CG. Experimental study of heat and mass transfer on an absorber with several enhancement tubes. Heat Transf Res 1999;28:664–74.
[26] Miller WA, Keyhani M. The correlation of simultaneous heat and mass transfer experimental data for aqueous lithium bromide vertical falling film absorption. J Sol Energy Eng 2001;123:30.
[27] Matsuda A, Choi KH, Hada K, Kawamura T. Effect of pressure and concentration on performance of a vertical falling-film type of absorber and generator using lithium bromide aqueous solutions. Int J Refrig 1994;17:538–42.
[28] Choudhury SK, Hisajima D, Ohuchi T, Nishiguchi A, Fukushima T, Sakaguchi S. Absorption of vapors into liquid films flowing over cooled horizontal tubes. ASHRAE Trans 1993;99:81–9.
[29] Jeong S, Garimella S. Falling-film and droplet mode heat and mass transfer in a horizontal tube LiBr/water absorber. Int J Heat Mass Transf 2002;45:1445–58.
[30] Sultana P, Wijeysundera NE, Ho JC, Yap C. Modeling of horizontal tube-bundle absorbers of absorption cooling systems. Int J Refrig 2007;30:709–23.
[31] Islam MR. Absorption process of a falling film on a tubular absorber: an experimental and numerical study. Appl Therm Eng 2008;28:1386–94.
[32] Yoon J-I, Phan TT, Moon C-G, Lee H-S, Jeong S-K. Heat and mass transfer characteristics of a horizontal tube falling film absorber with small diameter tubes. Heat Mass Transf 2007;44:437–44.
[33] Kiyota M, Morioka I, Matsuyama T. Steam absorption into aqueous lithium bromide solution films falling inside vertical pipes. Heat Transf Res 2003;32:740–52.
[34] Bo S, Ma X, Chen H, Lan Z. Numerical simulation on vapor absorption by wavy lithium bromide aqueous solution films. Heat Mass Transf 2011;47:1611–9.
[35] Patnik V, Perez-Blanco H. WAR. A simple analytical model for the design of vertical tube absorbers. ASHRAE Trans 1993;99:69–80.
[36] Medrano M, Bourouis M, Coronas A. Absorption of water vapour in the falling film of water–lithium bromide inside a vertical tube at air-cooling thermal conditions. Int J Therm Sci 2002;41:891–8.
[37] Karami S, Farhanieh B. A numerical study on the absorption of water vapor into a film of aqueous LiBr falling along a vertical plate. Heat Mass Transf 2009;46:197–207.
[38] Yang Z, Matsumoto S, Goto H, Matsumoto M, Maeda R. Ultrasonic micromixer for microfluidic systems 2001;93:266–72.
[39] El Moctar AO, Aubry N, Batton J. Electro-hydrodynamic micro-fluidic mixer. Lab Chip 2003;3:273–80.
[40] Glasgow I, Aubry N. Enhancement of microfluidic mixing using time pulsing. Lab Chip 2003;3:114–20.
[41] Stroock AD, Dertinger SKW, Ajdari A, Mezic I, Stone H a, Whitesides GM. Chaotic mixer for microchannels. Science 2002;295:647–51.
[42] Aref H. Chaotic advection of fluid particles. Philos Trans Phys Sci Eng 1990;333:273–88.
[43] Mortazavi M, Moghaddam S. Scalable bonding of polytetrafluoroethylene (ePTFE) nanofibrous membranes on microstructures. Enabling nanofabrication rapid innov. California: Work. Napa; August 18–21, 2013.
[44] Vincenti WG, Kruger CH. Introduction to physical gas dynamics. Krieger Pub Co; 1975.
[45] Beskok A, Karniadakis GE. A model for flows in channels, pipes, and ducts at micro and nano scales. Microscale Thermophys Eng 1999;3:43–77.
[46] Mason EA, Malinauskas AP. Gas transport in porous media: the dusty-gas model. New York: Elsevier Scientific Pub; 1983.
[47] Kyung I, Herold KE, Kang YT. Model for absorption of water vapor into aqueous LiBr flowing over a horizontal smooth tube. Int J Refrig 2007;30:591–600.
[48] Bo S, Ma X, Lan Z, Chen J, Chen H. Numerical simulation on the falling film absorption process in a counter-flow absorber. Chem Eng J 2010;156:607–12.
[49] Papaefthimiou VD, Koronaki IP, Karampinos DC, Rogdakis ED. A novel approach for modelling LiBr–H_2O falling film absorption on cooled horizontal bundle of tubes. Int J Refrig 2012;35:1115–22.
[50] McNeely LA. Thermodynamic properties of aqueous solutions of lithium bromide. ASHRAE Trans 1979;85:413–34.
[51] Yu D, Ladd AJC. A numerical simulation method for dissolution in porous and fractured media. J Comput Phys 2010;229:6450–65.
[52] McNamara G, Zanetti G. Use of the Boltzmann equation to simulate lattice-gas automata. Phys Rev Lett 1988;61:2332–5.
[53] He X, Luo L. A priori derivation of the lattice Boltzmann equation. Phys Rev E 1997;55:6333–6.